LA-UR-16-20128 (Accepted Manuscript)

Temperature dependence of the radiation tolerance of nanocrystalline pyrochlores A2Ti2O7 (A = Gd, Ho and Lu)

Wen, Juan
Sun, Cheng
Dholabhai, Pratik
Xia, Y.
Tang, Ming
Chen, Di
Yang, D.Y.
Li, Y.H.
Uberuaga, Blas P.
Wang, Yongqiang

To be published in: Acta Materialia

DOI to publisher's version: 10.1016/j.actamat.2016.03.025

Permalink to record: http://permalink.lanl.gov/object/view?what=info:lanl-repo/lareport/LA-UR-16-20128

Temperature dependence of the radiation tolerance of nanocrystalline pyrochlores $A_2Ti_2O_7$ (A = Gd, Ho and Lu)

J. Wen [a, b], C. Sun [b], P.P. Dholabhai [b], Y. Xia [a], M. Tang [b], D. Chen [b], D.Y. Yang [a], Y.H. Li [a,*], B.P. Uberuaga [b,*], Y.Q. Wang [b,*]

[a] *School of Nuclear Science and Technology, Lanzhou University, Lanzhou, Gansu 730000, China*

[b] *Materials Science and Technology Division, Los Alamos National Laboratory, Los Alamos, NM 87545, USA*

* *Corresponding author E-mail address:*

liyuhong@lzu.edu.cn (Y.H. Li), blas@lanl.gov (B.P. Uberuaga) and yqwang@lanl.gov (Y.Q. Wang)

Abstract

A potentially enhanced radiation resistance of nanocrystalline materials, as a consequence of the high density of interfaces and surfaces, has attracted much attention both to understand the fundamental role of these defect sinks and to develop them for high-radiation environments. Here, irradiation response of nanocrystalline $A_2Ti_2O_7$ (A = Gd, Ho and Lu) pyrochlore powders with grain sizes of 20-30 nm was investigated by 1-MeV Kr^{2+} ion bombardment. *In situ* transmission electron microscopy (TEM) revealed that the critical amorphization fluence for each nanocrystalline compound at room temperature was greater than that for their coarse-grained counterparts, indicating an enhanced amorphization resistance. The effect of temperature on the irradiation response of one of these compounds, nanocrystalline $Lu_2Ti_2O_7$, was further examined by performing ion irradiation at an elevated temperature range of 480 to 600 K. The critical amorphization temperature (T_c) was found to be noticeably higher in nanocrystalline $Lu_2Ti_2O_7$ (610 K) than its coarse-grained counterpart (480 K), revealing that nanocrystalline $Lu_2Ti_2O_7$ is less resistant to amorphization compared to its coarse-grained phase under high temperatures. We interpret these results with the aid of atomistic simulations. Molecular statics calculations find that

cation antisite defects are less energetically costly to form near surfaces than in the bulk, suggesting that the nanocrystalline form of these materials is generally less susceptible to amorphization than coarse-grained counterparts at low temperatures where defect kinetics are negligible. In contrast, at high temperatures, the annealing efficiency of antisite defects by cation interstitials is significantly reduced due to the sink properties of the surfaces in the nanocrystalline pyrochlore, which contributes to the observed higher amorphization temperature in the nano-grained phase than in coarse-grained counterpart. Together, these results provide new insight into the behavior of nanocrystalline materials under irradiation.

Keywords: Nanocrystalline; Pyrochlores; Cation antisite defects; Critical amorphization fluence; Radiation damage.

1. Introduction

Nanocrystalline materials, which consist of single or multiple phases with crystal grain sizes less than 100 nm in at least one dimension compared to conventional polycrystals, have received considerable attention owing to their outstanding physical, mechanical and chemical properties [1-3]. In particular, because of the high density of interfaces and surfaces, these materials often exhibit enhanced radiation tolerance and thus are attractive for application in various radiation environments. Upon irradiation, energetic particles interact with atoms of the target materials and create collision cascades on the picosecond time scale. This process unavoidably induces a large number of point defects, such as interstitials (*i*) and vacancies (*v*), which can aggregate to form extended defects, such as clusters, dislocation loops and voids [4-7]. These defects cause microstructure changes (swelling, amorphization etc.) and eventually lead to severe degradation of the material properties (hardening, embrittlement etc.). In order to increase the radiation

tolerance of materials, the fundamental goal is to suppress the accumulation of radiation-induced point defects in grain interiors. Incorporating solid-vapor and solid-solid interfaces during materials synthesis is one promising route to reduce the defect content in these materials, which provide a shorter diffusion distance between point defects and nearby interfaces/surfaces where they can be readily absorbed or annihilated. Nanocrystalline materials have shown enhanced radiation tolerance to amorphization relative to their coarse-grained counterparts simply because they have significantly larger interfaces/surfaces area working as effective sinks to absorb or annihilate radiation-induced point defects. Experiments on ion-irradiated nanocrystalline solids Pd and ZrO_2 by Rose et al., for example, found that the point defect density was reduced by a factor of 3-4 when the specimen grain size was reduced from ~100 nm to ~40 nm, and furthermore no defects were observed in the smallest ZrO_2 (< 15 nm) and Pd (< 30 nm) grains [8, 9]. A nanocrystalline NiTi alloy irradiated by 1.5 MeV Ar^+ ions retained its long-range order up to the twice the irradiation dose that would have led to significant amorphization of its coarse-grained counterpart [10]. Furthermore, Shen et al. reported that nanocrystalline $MgGa_2O_4$ spinel resisted amorphization doses up to 96 displacements per atom (dpa) which is at least 8 times higher than that needed to amorphize its coarse-grained counterpart [11]. These experimental results were consistent with the expectation of enhanced radiation resistance on nanostructured materials. Indeed, molecular dynamics simulations have shown that the defect-interface interaction strongly affects the primary radiation damage stage, with the interface acting as a sink to effectively annihilate defects and thus facilitating self-healing of the radiation-induced damage [12, 13]. However, Meldrum et al. found that nanocrystalline ZrO_2 embedded in a SiO_2 matrix is readily amorphized while bulk ZrO_2 has never been made amorphous by ion irradiation [14]. The experimental results reported by Chimi et al. further show that the defect accumulation rate in

nano-Au was significantly affected by temperature [15]. These observations indicate that nano is not always better than bulk phase, and temperature could remarkably affect the radiation behavior of the nano materials.

In the context of nuclear materials, pyrochlore oxides with the general formula $A_2B_2O_7$ are of particular interest, because they have been proposed as potential host matrices for the immobilization of fission products and actinides [16-22]. The structure of pyrochlore is isometric ($Fd\bar{3}m$, Z = 8, and a = 9-12 Å) and is a derivative of the fluorite structure (MO_2, $Fm3m$) (shown in Fig. 1), except that cations are ordered on the A and B sites and one-eighth of the anions are missing, to compensate the reduced charge of the A^{3+} cations. The eight-coordinated A sites (16*c*) located within a distorted cubic coordination polyhedron are typically occupied by trivalent actinides and lanthanides, whereas the six-coordinated B sites (16*d*) located within a distorted octahedron are usually occupied by a smaller cation, such as Ti, Zr, Hf, or Sn [23, 24]. There are three unique anion sites, 48*f*, 8*a* and 8*b*, in the pyrochlore structure. The 48*f*-site is coordinated with two B^{4+} cations and A^{3+} cations, while the 8*b*-site is in a tetrahedral coordination with four A^{3+} cations. The 8*a*-anion site is unoccupied and surrounded by four B^{4+} cations; these structural "vacancies" at the 8*a* site are ordered on the anion sublattice [25, 26]. When actinides are substituted into the A-site of the pyrochlore structure, radiation damage by α decays (~5 MeV) and their accompanying heavy recoils (~80 keV) from the incorporated actinides can cause structural changes and may eventually deteriorate its long-term performance as a stable host material for nuclear waste immobilization [27, 28]. Therefore, understanding the behavior of pyrochlore under various types of irradiation has important implications. Previous studies revealed that the irradiation responses of pyrochlores vary significantly as a function of composition [29-33]. In addition, atomistic computer simulations have shown that the cation antisite pair is the most

stable defect in the pyrochlore structure, and further revealed that cation antisite defects and disordering of the pyrochlore structure are generally responsible for the observed lattice swelling and amorphization [16, 34-36]. That is, when the formation energy for cation disorder increases with changing A or B cation chemistry, the pyrochlore resistance to amorphization decreases [16]. In particular, in the titanate series, $Gd_2Ti_2O_7$ exhibits the least amorphization resistance and has the highest disordering energy [36].

Despite the fact that a large number of publications have been devoted to understanding the irradiation-induced crystalline-to-amorphous (c-a) phase transformation in mostly coarse-grained pyrochlores, the effects of grain size on the c-a phase transformation in pyrochlore have not been systematically investigated. To the best of our knowledge, there has been only one recent report in which the nanocrystalline pyrochlore $Gd_2(Ti_{0.65}Zr_{0.35})_2O_7$ was found to display a greater radiation resistance as compared to its coarse-grained counterpart at room temperature [37]. Although those authors showed an enhanced resistance in nanocrystalline $Gd_2(Ti_{0.65}Zr_{0.35})_2O_7$, detailed information about the irradiation behavior, i.e., accumulation and recovery of radiation-induced defects under different irradiation temperatures, were not presented. In the present study, we first investigated the extent of ion radiation induced damage in several nanocrystalline pyrochlores $A_2Ti_2O_7$ (A = Gd, Ho and Lu) by *in situ* transmission electron microscopy (TEM) at room temperature. Second, the effect of temperature on the irradiation response was further examined in nanocrystalline $Lu_2Ti_2O_7$ by performing ion irradiation at an elevated temperature range of 480 to 600 K. Atomistic calculations were used to interpret the experimental observations, both at low and high temperatures. These new results provide important insight into the dynamic processes of defects and the effect of nanostructure on the radiation tolerance of pyrochlores.

2. Methods

2.1 Sample synthesis and TEM specimen preparation

Nanocrystalline pyrochlore powders of $A_2Ti_2O_7$ (A = Gd, Ho and Lu) were synthesized by the citric acid sol-gel route using the specific rare-earth oxide (RE_2O_3, 99.99%) and tetrabutyl titanate as starting materials with the molar rate of RE/Ti at 1:1. Anhydrous citric acid (CA) and absolute ethanol were used as chelator and solvent, respectively. The amount of citric acid was determined at $n_{CA}/(n_A+n_{Ti}) = 2.5$. To find appropriate fabrication temperatures for each composition with pyrochlore phase and desired grain size, we synthesized a set of samples for each composition in a temperature range of 750 to 850 ^oC with a step size of 20 ~30 ^oC. The samples reported here are prepared with the following conditions. The precursors of $A_2Ti_2O_7$ (A = Gd, Ho and Lu) were heated in air at 800 ^oC for both $Gd_2Ti_2O_7$ and $Ho_2Ti_2O_7$ and 830 ^oC for $Lu_2Ti_2O_7$, with the same dwelling time of 1 h, followed by furnace cooling down to room temperature naturally. Crystal structures were analyzed using a Rigaku D/Max-2400 X-ray Diffractometer with Cu-$K\alpha$ radiation of wavelength λ = 1.5406 Å. The θ-2θ scans in the range of 10-80^o were performed using a step size of 0.02^o and a dwell time of 4 seconds per step. Before the irradiation, the average grain size of nanocrystalline $A_2Ti_2O_7$ (A = Gd, Ho and Lu) pyrochlore powders was determined by a FEI Tecnai F30 transmission electron microscopy. A Hitachi H-9000NAR transmission electron microscope was used to study phase transformations during the in-situ ion irradiation experiments. TEM samples were prepared by dispersing the resulting powder into absolute ethanol using ultrasonic treatment, then dropping the solution onto the carbon-coated TEM grids and naturally drying in air.

2.2 Ion beam irradiation and *in situ* TEM characterization

Ion irradiation and *in situ* TEM observations were performed using the Intermediate Voltage Electron Microscopy (IVEM)-Tandem Facility at Argonne National Laboratory with 1 MeV Kr^{2+} ions under a temperature range of room temperature (293 K) to 600 K. A constant ion flux of 6.25×10^{11} ions/cm^2/s was used to minimize irradiation-induced temperature changes during all irradiation experiments. Specimens were bombarded by the ion beam at an angle 30^o off the electron beam direction. During the irradiation, the electron beam was blocked to avoid concurrent electron beam irradiation damage. The temperature was monitored by a thermocouple connected to the TEM holder. The c-a phase transformation induced by Kr ions was detected by *in situ* TEM imaging and selected area electron diffraction (SAED) patterns. The point of complete amorphization occurrence, at which the critical amorphization fluence (F_c) is defined, was determined by the disappearance of all of the diffraction intensities in the SAED patterns. To determine whether the irradiated region is fully amorphized, we either used the beam mask to block the 000 spot or lowered the beam intensity to observe the weak diffraction spots depending on the diffraction intensities from a specific specimen. We also took electron diffraction patterns from different parts of the specimen to make sure the material is fully amorphized under the stated amorphization fluence.

The critical amorphization fluence in the unit of displacements per atom (the amorphization dose, D_c (dpa)), was estimated using SRIM (Stopping and Range of Ions in Matter) simulations with the full-cascade mode assuming 50 eV threshold displacement energies for all elements Gd, Ho, Lu, Ti, and O in our titanate pyrochlores [38]. The incident projectile range of 1-MeV Kr^{2+} ions is ~ 300 nm, greater than the typical TEM sample thickness. Therefore, most of Kr ions pass through the TEM samples, and impurity effects of the implanted ions are negligible. It is important to emphasize that all irradiation parameters were chosen to match those in Ref. [31], as

we will compare our results to those, which were on large-grained pyrochlore samples. For a direct comparison, the dose determination for each ion fluence here also corresponds to a calculated dpa value at a depth of ~100 nm in the nanocrystalline specimen.

The critical amorphization temperature, T_c, is defined as the temperature at which the recrystallization rate is equal to the damage rate, and above which amorphization is not induced by the irradiation [31]. This temperature is deduced by the experimentally determined critical amorphization fluence (F_c). The equation used for F_c to T_c conversion [39] can be expressed by

$$F_c = \frac{F_0}{1-exp[(E_a/k_b)(1/T_c-1/T)]} \quad (1)$$

where F_0 is the amorphization fluence extrapolated to absolute zero − the point at which no annealing can occur and E_a is the activation energy for the dynamic annealing process during irradiation, using the Boltzmann constant (k_b = 8.617342 × 10^{-5} eV K^{-1}).

2.3 Atomistic simulations

To help interpret the experimental results, atomistic simulations were performed. Specifically, the formation energy of antisites as a function of distance from a surface of pyrochlore was determined. The atomistic simulations employed an empirical potential of the Buckingham form with parameterizations as provided by Ref. [40]. A model of the pyrochlore surface was constructed in a way that no surface dipoles were formed and that the model remained as a whole stoichiometric, and, as a consequence, charge neutral. The size of this stoichiometric slab model was 2.82 × 5.48 × 2.03 nm^3 (2640 atoms). To mimic the surface, a vacuum of 5 nm was added along the y axis (normal to the surface). This model was found to be stable upon annealing at 3000 K for 10 ns. Subsequently, the annealed structure was used for further calculations. Antisite formation energies

were calculated near the <110> surface of pyrochlore, which we determine to be the most stable of the low index surfaces. Details will appear in a forthcoming paper. Antisite pairs were created in each layer of the structure, one-by-one, as a function of distance from the surface. We also rely on recent simulations of the annealing of antisite defects by cation interstitials [41], as found using temperature accelerated dynamics, to provide further insight into the experimental observations.

3. Results and discussion

3.1 Characterization of pristine specimens by XRD and TEM

Measured X-ray diffraction patterns for pristine nanocrystalline $A_2Ti_2O_7$ (A = Gd, Ho and Lu) pyrochlores are shown in Fig. 2. Because pyrochlore is a superstructure of the fluorite structure, with an ordered arrangement of cations and oxygen vacancies, its pattern is composed of a set of principal diffraction maxima of the "parent" fluorite structure, and an additional set of "superlattice" reflections from the pyrochlore structure. Figure 2 shows that all of the compounds possess the pyrochlore structure, where the pyrochlore reflections, referred to as "superlattice" reflections, are labeled in the XRD patterns with the corresponding Miller indices of crystallographic planes. Diffraction peaks of P(222), P(400), P(440) and P(622), same as the parent fluorite reflections of F(111), F(200), F(220) and F(311), are attributable to both the pyrochlore and fluorite structures. Significant broadening of the peaks indicates the formation of ultrafine-grained structure. Thus, based on the full width at half maximum (FWHM) of the most intense peaks within the angle two theta range of $10^o \sim 60^o$ and using Scherrer's formula [42], we have determined that the average grain size in the pristine nanocrystalline $Gd_2Ti_2O_7$, $Ho_2Ti_2O_7$ and $Lu_2Ti_2O_7$ specimens are approximately 25.2 nm, 20.4 nm and 22.5 nm, respectively.

Dark field TEM images and SAED patterns in the insets for the pristine nanocrystalline $Gd_2Ti_2O_7$, $Ho_2Ti_2O_7$ and $Lu_2Ti_2O_7$, are shown in Fig. 3 (a-c), respectively. The SAED patterns show characteristic nanocrystalline rings resulting from each compound. The indices labeled in the patterns further confirm that all the compounds exhibit pyrochlore structure, consistent with the XRD analysis. High-resolution TEM (HRTEM) images (Fig. 3 (d-f)) and the corresponding fast Fourier transforms (insets in Fig. 3(d-f)) confirm that the pyrochlore structure is formed in the individual grains. The lattice fringes with an interplanar distance (labeled in the HRTEM images) are attributed to the (331) plane of the pyrochlore structure. From the dark field TEM images, it can be found that the grain sizes are very similar, with an average diameter of ~ 28 nm for $Gd_2Ti_2O_7$, ~ 23 nm for $Ho_2Ti_2O_7$ and ~ 27 nm for $Lu_2Ti_2O_7$, consistent with XRD results. Grain size distributions for all compounds were found to be quite narrow as shown in Fig. 3(g-i).

3.2 Ion irradiation-induced amorphization as a function of composition

The nanocrystalline rare-earth titanate pyrochlores ($A_2Ti_2O_7$, A = Gd, Ho and Lu) were irradiated by *in situ* 1 MeV Kr^{2+} ions at room temperature, a relatively low temperature for these materials. A series of SAED patterns for the nanocrystalline $Gd_2Ti_2O_7$, $Ho_2Ti_2O_7$ and $Lu_2Ti_2O_7$ (shown in Fig. 4) were taken to monitor the phase transformation during ion irradiation. As an example, SAED patterns for the nanocrystalline $Gd_2Ti_2O_7$ (Fig. 4 (a-d)) were obtained at fluences of 1×10^{14} ions/cm^2 (0.12 dpa), 2×10^{14} ions/cm^2 (0.24 dpa), and 3×10^{14} ions/cm^2 (0.36 dpa). The SAED patterns show clear evidence of an irradiation-induced c-a phase transformation in the nanocrystalline $Gd_2Ti_2O_7$. With increasing irradiation fluence, the intensity of the diffraction maxima gradually decreases. Complete amorphization was achieved at a fluence (dose) of 3×10^{14} ions/cm^2 (0.36 dpa) based on the appearance of a broad and diffuse halo that is characteristic of amorphization in the SAED pattern.

A similar amorphization process was also observed for the nanocrystalline $Ho_2Ti_2O_7$ (shown in the Fig. 4 (e-h)) and $Lu_2Ti_2O_7$ (shown in the Fig. 4 (i-l)), which exhibited higher critical amorphization fluences (doses) of 3.75×10^{14} ions/cm^2 (0.53 dpa) and 6×10^{14} ions/cm^2 (0.81dpa), respectively. F_c (ions/cm^2) and D_c (dpa) at room temperature for nanocrystalline $A_2Ti_2O_7$ (A = Gd, Ho and Lu) are summarized in Table 1. By comparing ion irradiation in various pyrochlores with similar nanograin sizes, we found that the critical amorphization fluence increases with the sequence of the nanocrystalline $Gd_2Ti_2O_7$, $Ho_2Ti_2O_7$ and $Lu_2Ti_2O_7$, which exhibits the same trend as in coarse-grained titanate pyrochlores. The critical amorphization resistance values of coarse-grained pyrochlores (single crystals) conducted under the same ion irradiation conditions were reported in Ref. [31]. For comparison, these results were also listed in Table 1 and Fig. 5. The critical amorphization fluences for our nanocrystalline pyrochlores $A_2Ti_2O_7$ (A = Gd, Ho and Lu) at room temperature are consistently higher than those of the coarse-grained counterparts. On one hand, thermodynamic analysis shows that smaller grain size results in a larger area fraction of interfaces/surfaces and thus an increased free energy, which tends to reduce irradiation stability [43]. On the other hand, kinetically, since the high density of interfaces and surfaces act as sinks for the annihilation of radiation-induced defects, the radiation tolerance of materials can be improved [12]. These two competing effects normally determine the final irradiation performance. For the c-a transformation results presented in this section where the irradiation was performed under room temperature, defects are essentially immobile, suggesting thermodynamic effects may dominate while the kinetic effect is considered negligible. As discussed below, we propose that the enhanced radiation tolerance of the nanocrystalline pyrochlores is due to enhanced stability of cation antisites near pyrochlore surfaces. This model also provides insight into the c-a transformation results obtained at elevated temperatures as presented in the next section.

3.3 Irradiation response of nanocrystalline $Lu_2Ti_2O_7$ at elevated temperatures

To understand how the irradiation effects observed at room temperature translate to higher temperatures, nanocrystalline $Lu_2Ti_2O_7$ was irradiated with 1 MeV Kr^{2+} ions over the temperature range of 480 to 600 K. Fig. 6 (a) shows the sequence of dark field TEM images and associated SAED patterns in the insets from nanocrystalline $Lu_2Ti_2O_7$ irradiated at 480 K. The reduced contrast in the dark field images indicates the loss of crystallinity with ion fluence (dose) ranging from 3.75×10^{14} ions/cm^2 (0.51 dpa) to 6×10^{14} ions/cm^2 (0.81 dpa), while the intensity of the diffraction rings decreases gradually along with the emergence of an amorphous halo in the SAED patterns. These results reveal that the nanocrystalline $Lu_2Ti_2O_7$ underwent a c-a phase transformation when irradiated at 480 K. A similar c-a phase transformation was also observed under irradiation at 520 K as shown in Fig. 6 (b), where complete amorphization was achieved at a fluence (dose) of 6×10^{14} ions/cm^2 (0.81 dpa). As shown in Fig. 6 (c), however, when the irradiation temperature was raised to 600 K, the complete c-a phase transformation did not occur even at a much higher fluence (dose) of 2.5×10^{15} ions/cm^2 (3.38 dpa). Figures 4 (i-l) and 6 (a-c) demonstrate that, as the irradiation temperature increases, the critical amorphization fluence (dose) increases as a result of the enhanced recrystallization due to the more efficient dynamic annealing.

The critical amorphization fluence (F_c) for the nanocrystalline $Lu_2Ti_2O_7$ versus temperature is plotted in Fig. 5, along with that of coarse-grained $Lu_2Ti_2O_7$ from Ref. [31]. Based on Eq. (1), the critical amorphization temperature, T_c, and the activation energy of recrystallization, E_a, can be determined from the critical amorphization fluence versus temperature curve and are listed in Table 1. To check the validity of Eq. (1) [39] when estimating T_c and E_a in our experiments, we also applied a model proposed by Weber and his colleagues [44, 45] to determine T_c and E_a for

our nano-grained $Lu_2Ti_2O_7$. According to Weber's model, the critical amorphization dose, *D*, is related to temperature, *T*, by:

$$\ln(1 - D_0/D) = \ln(1/\emptyset\sigma\tau) - E_a/k_bT. \qquad (2)$$

Here D_0 is the cumulative dose to achieve amorphization at 0 K, ϕ is the ion beam flux, σ is the cascade damage cross section, and τ is a time constant for the annealing process. The critical amorphization temperature, T_c, can be derived from Eq. (2) when D approaches infinite,

$$T_c = E_a/[k_b \ln 1/\emptyset\sigma\tau] \qquad (3)$$

The Arrhenius-type plot of Equation 2, $\ln(1 - D_0/D6)$ vs. $1/k_bT$, using data from Fig. 5 yields $-E_a$ as the slope and $\ln(1/\emptyset\sigma\tau)$ as the Y-intercept, from which the critical amorphization temperature, T_c, can then be determined by Eq. (3). Using Eqs. (2) and (3), we obtained values of E_a and T_c to be 0.9 eV and 608 K respectively for the nano-grained $Lu_2Ti_2O_7$, which are very close to those listed in Table 1 based on Eq. (1) using the cascade-quench model [39].

The critical amorphization temperature, T_c, above which complete amorphization cannot occur, is useful to evaluate the susceptibility to radiation-induced amorphization of materials; higher T_c implies that the materials are more susceptible to amorphization. Fig. 5 indicates that the critical amorphization temperature increases from ~480 K for the coarse-grained $Lu_2Ti_2O_7$ to ~610 K for the nano-grained $Lu_2Ti_2O_7$, suggesting that the nano-grained $Lu_2Ti_2O_7$ is more susceptible to ion-beam induced amorphization. This finding is somewhat unexpected. In fact, quite an opposite conclusion was anticipated since all three pyrochlore composites have shown higher critical amorphization fluences (doses) in the nanocrystalline phase than the coarse-grained phase when the irradiation was performed at room temperature (as shown in Fig. 5). Conventional

understanding is that (1) surfaces act as an effective defect sink that reduces the defect concentration; and (2) at elevated temperatures the defects are more mobile and are more efficiently absorbed by the surface. This understanding implies that a nanocrystalline phase should be even more resistant to amorphization than its coarse-grained counterpart under elevated temperature irradiations as compared to the room temperature irradiation, in contrast to our experimental results. Different critical amorphization temperatures have been linked to the damage cascade size effect in previous studies [33], when pyrochlores are irradiated by ions with different masses. However, the damage cascade sizes should be very similar between the coarse-grained and nanocrystalline $Lu_2Ti_2O_7$ in our work, and such spectrum effects should not be the source of this surprising behavior at elevated temperatures. We should also mention that no noticeable grain growth in the nanocrystalline $Lu_2Ti_2O_7$ specimen was observed during the elevated temperature irradiations in this work.

3.4 Mechanisms for ion irradiation-induced defect evolution as a function of temperature

As outlined above, on the basis of the comparison of the distinct irradiation behavior for the nano- and coarse-grained $Lu_2Ti_2O_7$ pyrochlore between room temperature and elevated temperatures, different mechanisms are needed to explain the ion induced amorphization process at room and elevated temperatures. That is, to explain why the nanophased material exhibits enhanced radiation tolerance at lower temperature but degraded tolerance at elevated temperature. During ion irradiation, three types of fundamental point defects are created in pyrochlore oxides (for the sake of simplicity, extended defect clusters are not considered): cation antisite defects (A_B, B_A), vacancies (V_A, V_B, V_O) and interstitials (A_i, B_i, O_i) on the three sublattices A, B and O. Atomistic computer simulations have found that cation antisite defect are the most stable defect in the pyrochlore structure [16, 35, 36] and the comparison with experiments has correlated these defects

with the amorphization susceptibility of these materials [16]. A high concentration of defects can eventually lead to a loss of lattice periodicity, or amorphization. They also energetically destabilize the lattice, enhancing the tendency to be amorphized. Therefore, the formation of these defects and their migration and dynamic recovery determine the irradiation response of the pyrochlore structure.

At low temperatures, room temperature and below, where the critical amorphization fluence is independent of temperature, defects are effectively immobile. Thus, they are frozen where they are created and the response of the material is determined by the thermodynamics of the defects. While under irradiation, the dominant defects in pyrochlore seem to be cation antisites [35], other defects (interstitials and vacancies) may also form. How the energetics of these defects differs in nanophase pyrochlore as opposed to its larger-grained form then will dictate the response of the material. Figure 7 shows the relative formation energy of cation antisite pairs as a function of distance from a (110) surface of pyrochlore. These results clearly show that the formation energy is reduced as the defect is formed closer to the surface. We expect similar behavior for other types of defects. This indicates that, for equivalent volumes, a volume of pyrochlore that contains surfaces will, on average, have lower formation energies for cation antisites. Based on the ideas presented in Ref. [16] in which the susceptibility of pyrochlores to amorphization is related to the energetics of disordering, then the nanomaterial should exhibit superior resistance to amorphization, at least when defect thermodynamics dominate the response. That is, materials with a higher propensity to accommodate disorder tend to possess higher amorphization resistance. Thus, due to a much larger surface area in the nanocrystalline pyrochlore, a larger fluence is required to induce the amorphization transition as compared to the coarse-grained counterpart.

In contrast, as one approaches the critical amorphization temperature, defect kinetics becomes all important. The critical amorphization temperature is the temperature at which the dynamics of recrystallization are faster than the rate of defect formation. At these temperatures, cation interstitial defects become mobile and can anneal the antisite defects, while cation vacancies are still sluggish [41]. In pristine pyrochlore, the barrier for Lu interstitial migration is about 1.0 eV, while that for the Lu vacancy is 3.0-4.0 eV. Recent temperature accelerated dynamics simulations reveal that mobile cation interstitials can anneal cation antisites [41]. This suggests that cation interstitials are critical for determining the critical amorphization temperature and thus their availability dictates this temperature. As shown in Fig. 5, at ~480 K the nanophase $Lu_2Ti_2O_7$ is readily amorphized while the coarse-grained $Lu_2Ti_2O_7$ is resistant to amorphization. This means that the cation antisite defects (and any other defects) that are responsible for amorphization are not annealed efficiently by the cation interstitials. Thus, we conclude that cation interstitials are somehow eliminated from the system in the nanomaterial. The obvious culprit is the nearby surfaces. These will act as sinks for any mobile defect and, at these temperatures, the only mobile defects are cation interstitials. (We note that oxygen defects will certainly be mobile, but they are not able to reorder the cation sublattice and are thus not relevant to this discussion [46].) We speculate then that, while in the large-grained material cation interstitials become mobile and annihilate cation antisites at the critical amorphization temperature, in the nanomaterial these interstitials are swept to nearby surfaces, eliminating their ability to heal cation antisites. The same argument can be made for the annihilation of cation vacancies, which will also contribute to amorphization susceptibility. The proposed differences in radiation damage evolution in nano versus bulk pyrochlore at low and high temperatures are schematically illustrated in Fig. 8.

The critical amorphization temperature, ~610 K, above which the nanophase $Lu_2Ti_2O_7$ cannot be amorphized, represents a stage at which the dynamic annealing rate is persistently higher than the defect production rate. However, the defect annealing mechanism at this elevated temperature is not yet clear and is the subject of ongoing work.

An important unanswered question is why nanocrystalline spinel ($MgGa_2O_4$) exhibits vastly superior radiation tolerance compared to large grained material at low temperature [11], but only a small enhancement in radiation tolerance was observed in pyrochlore compounds when they were irradiated in a nanostructured form. At this stage, we can only suggest that this is a consequence of the nature of the "interfaces" in the two materials. In our pyrochlore samples, the material was characterized by a high fraction of free surfaces. In contrast, the spinel samples contained a high density of grain boundaries. It is possible that the grain boundaries are imperfect sinks, capturing and storing defects for eventual release back into the material in a manner similar to the so-called "interstitial emission" mechanism [12]. Surfaces, in contrast, act more as ideal sinks and thus these kinds of mechanisms are simply not possible. However, at the lower temperatures of the spinel experiments and our room temperature pyrochlore irradiations, defects are not diffusing to the grain boundaries and surfaces but must rather be created directly on the boundaries or surfaces via the collision cascade process. At this point, it is not clear if the difference between the two sets of experiments is a function of the different types of nanostructure (surfaces versus grain boundaries) or is due to some inherent difference in spinel as compared to pyrochlore. Thus, clearly more work is needed to elucidate the origins of radiation damage evolution in nanostructured materials.

4. Conclusions

In summary, we investigated the ion irradiation-induced phase transformation in nanocrystalline pyrochlore by *in situ* TEM over a range of temperatures. The irradiation response of nanocrystalline $A_2Ti_2O_7$ (A = Gd, Ho and Lu) at room temperature follows a similar trend to that of the coarse-grained counterparts in that the amorphization resistance increases with the sequence of $Gd_2Ti_2O_7$, $Ho_2Ti_2O_7$ and $Lu_2Ti_2O_7$, although all three nanocrystalline $A_2Ti_2O_7$ compounds exhibit slightly improved amorphization resistance than their coarse-grained counterparts at room temperature. At elevated temperatures, however, quite the opposite phenomenon is observed: coarse-grained $Lu_2Ti_2O_7$ shows greater amorphization resistance than its nanocrystalline phase. Atomistic simulations reveal that cation antisite defects are easier to form near surfaces than in the bulk. This overall decrease in the energetic penalty for cation disorder is responsible for enhanced radiation resistance at low temperature. At higher temperatures, cation interstitials, responsible for healing cation antisites, are annihilated at those same surfaces, reducing the healing efficiency. These results provide new insight into the role of interfaces and surfaces in the radiation tolerance of nanomaterials.

Acknowledgements

This work was partially supported by the National Natural Science Foundation of China (11175076 and 11475076) and the Fundamental Research Funds for the Central Universities of China (Lanzhou University, lzujbky-2015-bt07). The funding for Los Alamos National Laboratory (LANL) staff was provided by the US Department of Energy (DOE), Office of Basic Energy Sciences, Materials Sciences and Engineering Division and the Center for Integrated Nanotechnologies, a DOE user facility jointly operated by Los Alamos and Sandia National Laboratories. The electron microscopy with *in situ* ion irradiation was accomplished at Argonne National Laboratory at the IVEM-Tandem Facility, a U.S. Department of Energy Facility funded

by the DOE Office of Nuclear Energy, operated under Contract No. DE-AC02-06CH11357 by UChicago Argonne, LLC. We thank IVEM staff members including Dr. Meimei Li, Dr. Mark Kirk, Pete Baldo and Ed Ryan for assistance in the irradiation experiments. Partial support was also provided to J. Wen by the China Scholarship Council, a nonprofit organization affiliated with Ministry of Education of the People's Republic of China.

References

[1] T. Tsakalakos, I.A. Ovid'ko, A.K. Vasudevan. Nanostructures: Synthesis, Functional Properties and Application, Kluwer Academic Publishers, Dordrecht, Netherlands, 2003.
[2] K. Lu. Nanocrystalline metals crystallized from amorphous solids: nanocrystallization, structure, and properties, Mater. Sci. Eng. R: Reports 16 (1996) 161-221.
[3] N.R. Tao, Z.B. Wang, W.P. Tong, M.L. Sui, J. Lu, K. Lu. An investigation of surface nanocrystallization mechanism in Fe induced by surface mechanical attrition treatment, Acta Mater. 50 (2002) 4603-4616.
[4] B.D. Wirth. How does radiation damage materials?, Science 318 (2007) 923-924.
[5] K. Arakawa, K. Ono, M. Isshiki, K. Mimura, M. Uchikoshi, H. Mori. Observation of the one-dimensional diffusion of nanometer-sized dislocation loops, Science 318 (2007) 956-959.
[6] Y. Matsukawa, S.J. Zinkle. One-dimensional fast migration of vacancy clusters in metals, Science 318 (2007) 959-962.
[7] S.J. Zinkle, K. Farrell. Void swelling and defect cluster formation in reactor-irradiated copper, J. Nucl. Mater. 168 (1989) 262-267.
[8] M. Rose, G. Gorzawski, G. Miehe, A.G Balogh, H. Hahn. Phase stability of nanostructured materials under heavy ion irradiation, Nanostruct. Mater. 6 (1995) 731-734.
[9] M. Rose, A.G Balogh, H. Hahn. Instability of irradiation induced defects in nanostructured materials, Nucl. Instrum. Methods Phys. Res. B 127 (1997) 119-122.
[10] A.R. Kilmametov, D.V. Gunderov, R.Z. Valiev, A.G. Balogh, H. Hahn. Enhanced ion irradiation resistance of bulk nanocrystalline TiNi alloy, Scr. Mater. 59 (2008) 1027-1030.
[11] T.D. Shen, S.H. Feng, M. Tang, J.A. Valdez, Y.Q. Wang, K.E. Sickafus. Enhanced radiation tolerance in nanocrystalline $MgGa_2O_4$, Appl. Phys. Lett. 90 (2007) 263115.
[12] X.M. Bai, A.F. Voter, R.G. Hoagland, M. Nastasi, B.P. Uberuaga. Efficient annealing of radiation damage near grain boundaries via interstitial emission, Science 327 (2010) 1631-1634.
[13] D. Chen, J. Wang, T. Chen, L. Shao. Defect annihilation at grain boundaries in alpha-Fe, Sci. Rep. 3 (2013) 1450.
[14] A. Meldrum, L.A. Boatner, R.C. Ewing. Nanocrystalline zirconia can be amorphized by ion irradiation, Phys. Rev. Lett. 88 (2002) 025503.
[15] Y. Chimi, A. Iwase, N. Ishikawa, M. Kobiyama, T. Inami, S. Okuda. Accumulation and recovery of defects in ion-irradiated nanocrystalline gold, J. Nucl. Mater. 297 (2001) 355-357.
[16] K.E. Sickafus, L. Minervini, R.W. Grimes, J.A. Valdez, M. Ishimaru, F. Li, K.J. McClellan, T. Hartmann. Radiation Tolerance of Complex Oxides, Science 289 (2000) 748-751.

[17] R.C. Ewing, W.J. Weber, J. Lian. Nuclear waste disposal—pyrochlore ($A_2B_2O_7$): Nuclear waste form for the immobilization of plutonium and "minor" actinides, J. Appl. Phys. 95 (2004) 5949.
[18] W.J. Weber, R.C. Ewing, C.R.A. Catlow, T.D. De La Rubia, L.W. Hobbs, C. Kinoshita, Hj. Matzke, A.T. Motta, M. Nastasi, E.K.H. Salje, E.R. Vance, S.J. Zinkle. Radiation effects in crystalline ceramics for the immobilization of high-level nuclear waste and plutonium, J. Mater. Res. 13 (1998) 1434-1484.
[19] S.X. Wang, B.D. Begg, L.M. Wang, R.C. Ewing, W.J. Weber, K.V.G. Kutty. Radiation stability of gadolinium zirconate: a waste form for plutonium disposition, J. Mater. Res. 14 (1999) 4470-4473.
[20] W.J. Weber, R.C. Ewing. Radiation effects in crystalline oxide host phases for the immobilization of actinides. Mat. Res. Soc. Symp. Proc. vol. 713: Cambridge Univ Press, 2002. p.JJ3. 1.
[21] K.B. Helean, A. Navrotsky, E.R. Vance, M.L. Carter, B. Ebbinghaus, O. Krikorian, J. Lian, L.M. Wang, J.G. Catalano. Enthalpies of formation of Ce-pyrochlore, $Ca_{0.93}Ce_{1.00}Ti_{2.035}O_{7.00}$, U-pyrochlore, $Ca_{1.46}U^{4+}_{0.23}U^{6+}_{0.46}Ti_{1.85}O_{7.00}$ and Gd-pyrochlore, $Gd_2Ti_2O_7$: three materials relevant to the proposed waste form for excess weapons plutonium, J. Nucl. Mater. 303 (2002) 226-239.
[22] A.A. Digeos, J.A. Valdez, K.E. Sickafus, S. Atiq, R.W. Grimes, A.R. Boccaccini. Glass matrix/pyrochlore phase composites for nuclear wastes encapsulation , J. Mater. Sci. 38 (2003) 1597-1604.
[23] M.A. Subramanian, G. Aravamudan, G.V.S. Rao. Oxide pyrochlores—a review, Prog. Solid St. Chem. 15 (1983) 55-143.
[24] B.C. Chakoumakos. Systematics of the pyrochlore structure type, ideal $A_2B_2X_6Y$, J. Solid State Chem. 53 (1984) 120-129.
[25] P.J. Wilde, C.R.A. Catlow. Defects and diffusion in pyrochlore structured oxides, Solid State Ionics 112 (1998) 173-183.
[26] P.J. Wilde, C.R.A. Catlow. Molecular dynamics study of the effect of doping and disorder on diffusion in gadolinium zirconate, Solid State Ionics 112 (1998) 185-195.
[27] G.R. Lumpkin, R.C. Ewing. Alpha-decay damage in minerals of the pyrochlore group, Phys. Chem. Minerals 16 (1988) 2-20.
[28] W.J. Weber, J.W. Wald, Hj. Matzke. Self-radiation damage in $Gd_2Ti_2O_7$, Mater. Lett. 3 (1985) 173-180.
[29] G. Sattonnay, S. Moll, L. Thomé, C. Legros, M. Herbst-Ghysel, F. Garrido, J.-M. Costantini, C. Trautmann. Heavy-ion irradiation of pyrochlore oxides: Comparison between low and high energy regimes, Nucl. Instrum. Methods Phys. Res. B 266 (2008) 3043-3047.
[30] G. Sattonnay, N. Sellami, L. Thomé, C. Legros, C. Grygiel, I. Monnet, J. Jagielski, I. Jozwik-Biala, P. Simon. Structural stability of $Nd_2Zr_2O_7$ pyrochlore ion-irradiated in a broad energy range, Acta Mater. 61 (2013) 6492-6505.
[31] J. Lian, J. Chen, L.M. Wang, R.C. Ewing, J.M. Farmer, L.A. Boatner, K.B. Helean. Radiation-induced amorphization of rare-earth titanate pyrochlores, Phys. Rev. B 68 (2003) 134107.
[32] J. Lian, K.B. Helean, B.J. Kennedy, L.M. Wang, A. Navrotsky, R.C. Ewing. Effect of structure and thermodynamic stability on the response of lanthanide stannate pyrochlores to ion beam irradiation, J. Phys. Chem. B 110 (2006) 2343-2350.

[33] S.X. Wang, L.M.Wang, R.C. Ewing, G.S. Was, G.R. Lumpkin. Ion irradiation-induced phase transformation of pyrochlore and zirconolite. Nucl. Instrum. Methods Phys. Res. B 148 (1999) 704-709.
[34] K.E. Sickafus, R.W. Grimes, J.A. Valdez, A. Cleave, M. Tang, M. Ishimaru, S.M. Corish, C.R. Stanek, B.P. Uberuaga. Radiation-induced amorphization resistance and radiation tolerance in structurally related oxides, Nat. Mater. 6 (2007) 217-223.
[35] Y.H. Li, B.P. Uberuaga, C. Jiang, S. Choudhury, J.A. Valdez, M.K. Patel, J. Won, Y.Q. Wang, M. Tang, D.J. Safarik, D.D. Byler, K.J. McClellan, I.O. Usov, T. Hartmann, G. Baldinozzi, K.E. Sickafus. Role of Antisite Disorder on Preamorphization Swelling in Titanate Pyrochlores, Phys. Rev. Lett. 108 (2012) 195504.
[36] C. Jiang, C.R. Stanek, K.E. Sickafus, B.P. Uberuaga. First-principles prediction of disordering tendencies in pyrochlore oxides, Phys. Rev. B 79 (2009) 104203.
[37] J.M. Zhang, J. Lian, A.F. Fuentes, F.X. Zhang, M. Lang, F.Y. Lu, R.C. Ewing. Enhanced radiation resistance of nanocrystalline pyrochlore $Gd_2(Ti_{0.65}Zr_{0.35})_2O_7$, Appl. Phys. Lett. 94 (2009) 243110.
[38] J.F. Ziegler, J.P. Biersack, U. Littmark. Stopping and Range of Ions in Solids, Pergamon Pres, New Tork, 1985.
[39] S.X. Wang, L.M. Wang, R.C. Ewing. Irradiation-induced amorphization: Effects of temperature, ion mass, cascade size, and dose rate, Phys. Rev. B 63 (2000) 024105.
[40] L. Minervini, R.W. Grimes, K.E. Sickafus. Disorder in pyrochlore oxides, J. Am. Ceram. Soc., 83 (2000) 1873-1878.
[41] B.P. Uberuaga, R. Perriot. Insights into dynamic processes of cations in pyrochlores and other complex oxides, Phys. Chem. Chem. Phys. 17 (2015) 24215-24223.
[42] B.D. Cullity, S.R. Stock. Elements of X-ray Diffraction, Prentice hall Upper Saddle River, NJ, 2001.
[43] T.D. Shen. Radiation tolerance in a nanostructure: Is smaller better?, Nucl. Instrum. Methods Phys. Res. B 266 (2008) 921-925.
[44] W.J. Weber, "Models and mechanisms of irradiation-induced amorphization in ceramics, NIM B 166-167 (2000) 98-106.
[45] W.J. Weber, R.C. Ewing, and L.M. Wang, "The radiation-induced crystalline-to-amorphous transition in zircon, JMR 9 (1994) 688-698.
[46] R. Perriot, B.P. Uberuaga. Structural vs. intrinsic carriers: contrasting effects of cation chemistry and disorder on ionic conductivity in pyrochlores, J. Mater. Chem. A 3 (2015) 11554-11565.

Compositions	A^{3+} ionic radius (Å)	r_A/r_B	Lattice parameter (Å)	Density (g/cm^3)	Ion range (nm)	F_c at 293 K ($\times 10^{14}$ ions/cm^2)	D_c at 293 K (dpa)	T_c (K)	E_a (eV)
nano-$Gd_2Ti_2O_7$	**1.053**	**1.74**	**10.184**	**6.35**	**281.3**	**3.0**	**0.36**	**-**	**-**
$Gd_2Ti_2O_7$	1.053	1.74	10.186	6.567	267.9	1.5	0.18	1120	1
nano-$Ho_2Ti_2O_7$	**1.015**	**1.68**	**10.100**	**6.73**	**273.5**	**3.75**	**0.53**	**-**	**-**
$Ho_2Ti_2O_7$	1.015	1.68	10.104	6.926	263.9	1.93	0.27	850	0.3
nano-$Lu_2Ti_2O_7$	**0.977**	**1.61**	**10.015**	**7.16**	**277.4**	**6.0**	**0.81**	**610**	**0.8**
$Lu_2Ti_2O_7$	0.977	1.61	10.017	7.288	274	4.063	0.55	480	0.6

Table 1. Structural parameters of nanocrystalline (nano-) $A_2Ti_2O_7$ (A = Gd, Ho and Lu) pyrochlore obtained from refinements of X-ray diffraction data. Important parameters defining the irradiation response of these materials are also presented, including the amorphization fluence at 293 K, F_c; the critical amorphization temperature, T_c; and the activation energy of defect annealing, E_a, for nanocrystalline $A_2Ti_2O_7$ (A = Gd, Ho and Lu) (in bold). The amorphization dose, D_c (dpa), was calculated by SRIM as described in the main text. The values of the coarse-grained pyrochlores are taken from Ref. [31] with permission.

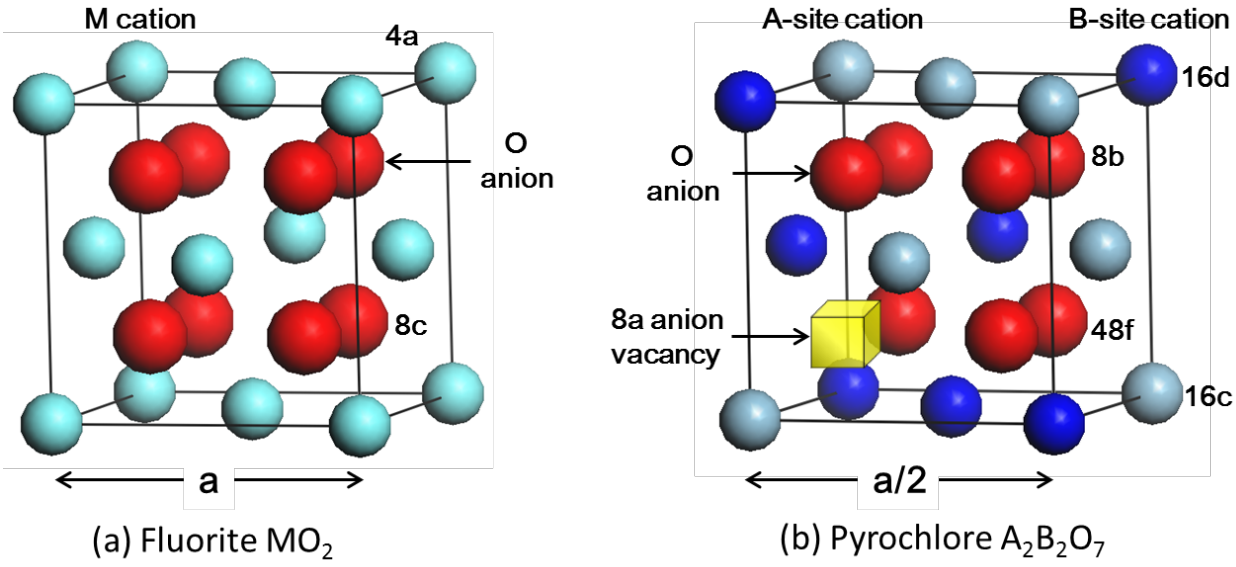

Fig. 1. Schematic drawing comparing the crystal structures of ideal fluorite (MO_2; M = cation) and pyrochlore ($A_2B_2O_7$; A, B = cations). The various atomic sites in the crystal structure are indicated by Wycoff notation. (a) Unit cell for the ideal fluorite crystal structure. The small light blue spheres represent metal cations. The large red spheres represent oxygen anions. (b) One eighth of the unit cell for the pyrochlore crystal structure. A^{3+} cations (shown as gray spheres) and B^{4+} cations (shown as dark blue spheres) have an ordered arrangement on the pyrochlore cation sublattice. Charge-compensation for these replacements is achieved by the introduction of oxygen vacancies (indicated as a yellow cube). These oxygen vacancies are ordered on the pyrochlore anion sublattice.

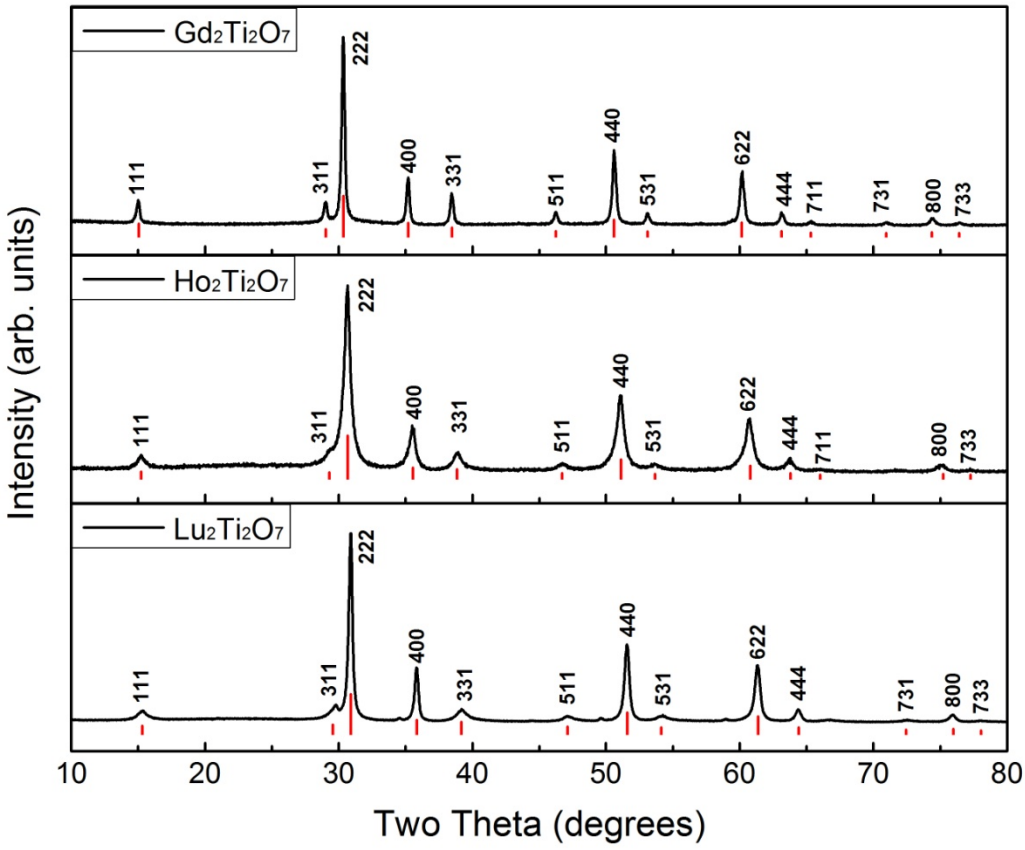

Fig. 2. XRD patterns obtained from pristine nanocrystalline $Gd_2Ti_2O_7$, $Ho_2Ti_2O_7$ and $Lu_2Ti_2O_7$ pyrochlore samples. Red vertical drop lines are standard XRD patterns for each composition.

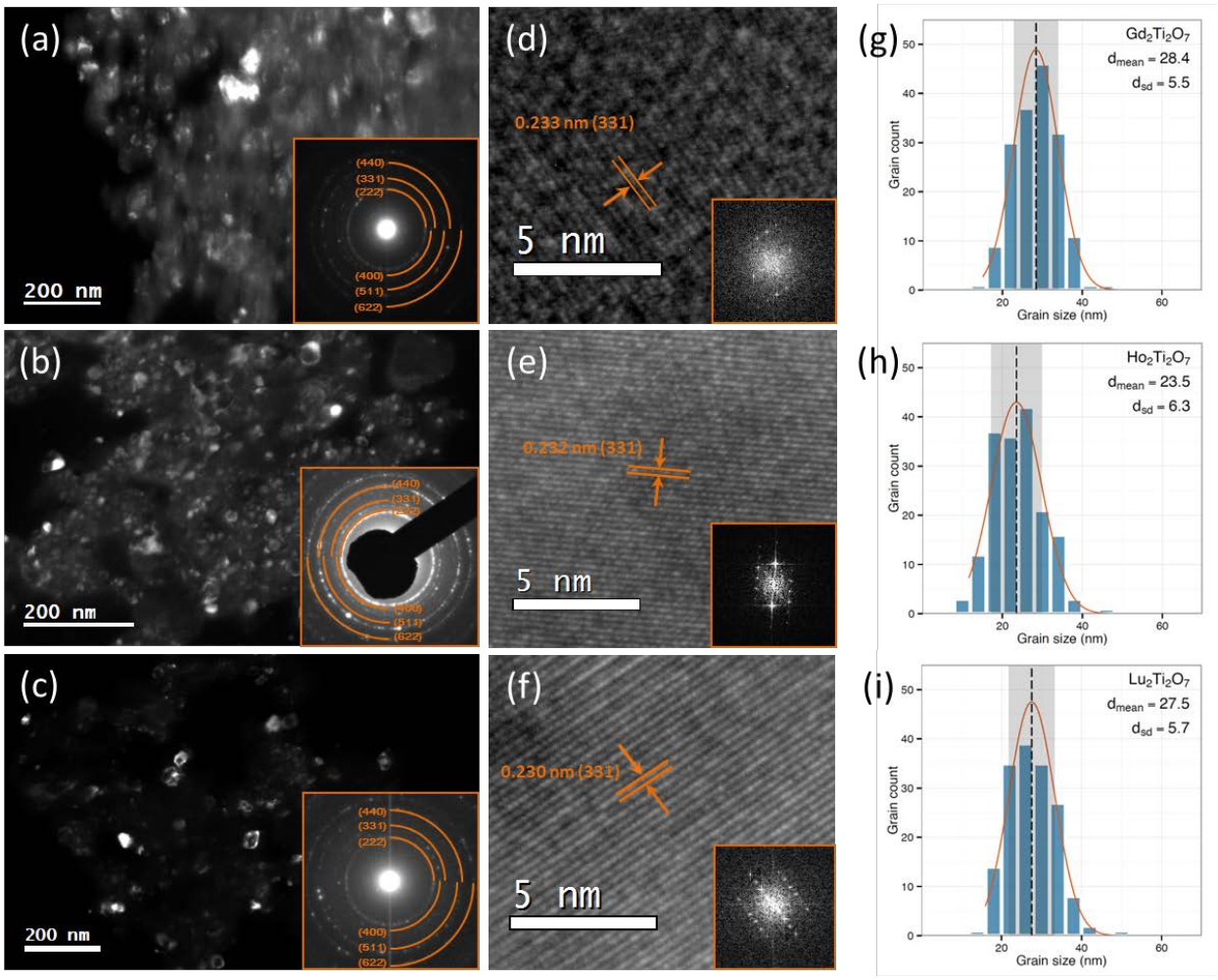

Fig. 3. TEM images and grain size histograms of pristine nanocrystalline $A_2Ti_2O_7$ (A = Gd, Ho and Lu) pyrochlore. (a)-(c) Dark field TEM images of pristine nanocrystalline $Gd_2Ti_2O_7$, $Ho_2Ti_2O_7$ and $Lu_2Ti_2O_7$ pyrochlores, respectively. The insets are the corresponding SAED patterns. (d)-(f) HRTEM images of nanocrystalline $A_2Ti_2O_7$ (A = Gd, Ho and Lu) pyrochlores with the associated FFT in the insets. Grain size histograms show the average grain size is (g) ~ 28.4 nm for $Gd_2Ti_2O_7$, (h) ~ 23.5 nm for $Ho_2Ti_2O_7$, and (i) ~ 27.5 nm for $Lu_2Ti_2O_7$.

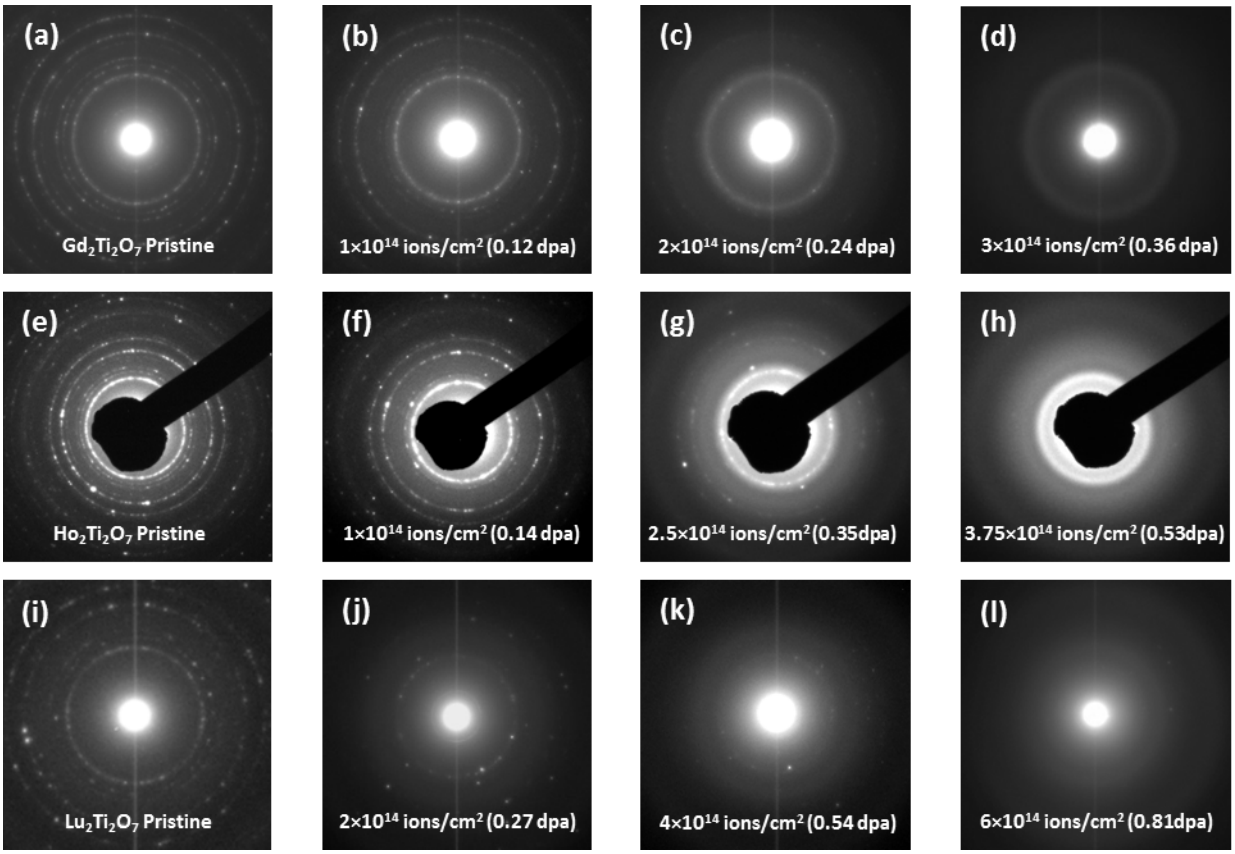

Fig. 4. Sequence of selected area diffraction patterns for nanocrystalline $A_2Ti_2O_7$ (A = Gd, Ho and Lu) pyrochlore taken during *in situ* 1 MeV Kr^{2+} ion irradiations at 293 K. The patterns of nanocrystalline $Gd_2Ti_2O_7$ (a-d), $Ho_2Ti_2O_7$ (e-h) and $Lu_2Ti_2O_7$ (i-l) indicate an ion irradiation-induced amorphization process. The ion fluences and dose in dpa are given in the bottom of each panel.

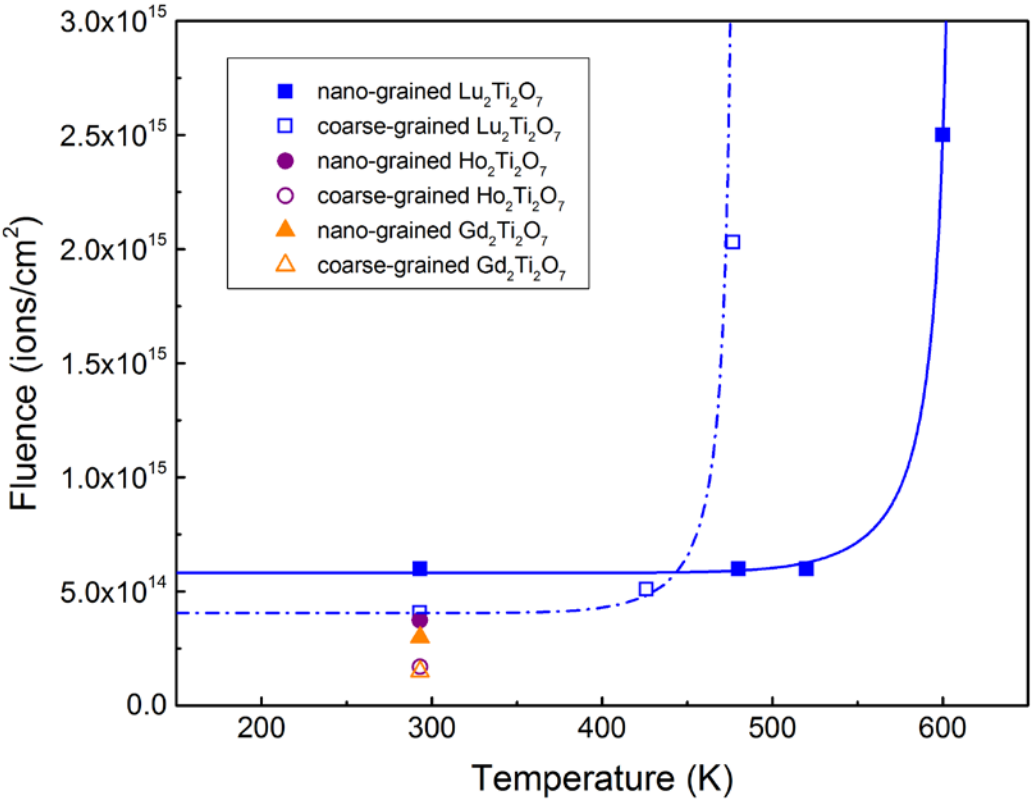

Fig. 5. Temperature dependence of the critical amorphization fluence (F_c) for nano-grained and coarse-grained $A_2Ti_2O_7$ (A = Gd, Ho and Lu) pyrochlore under 1 MeV Kr^{2+} ion irradiation. The curves are fitted using Eq. (1). The values of the coarse-grained titanate pyrochlores are taken from Ref. [31] with permission. The critical amorphization temperature, T_c, and activation energy, E_a, obtained from the curve fitting are listed in Table. 1.

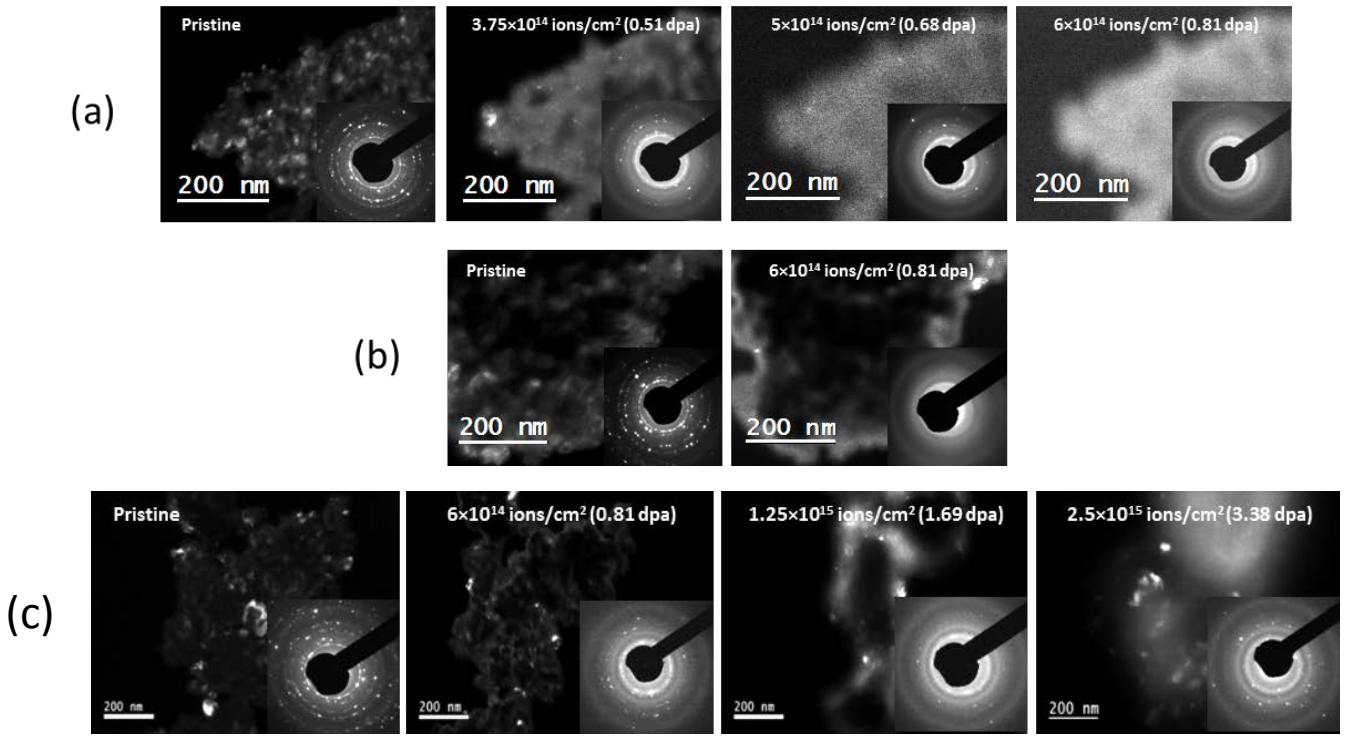

Fig. 6. Sequence of dark field TEM images and associated SAED patterns for nanocrystalline $Lu_2Ti_2O_7$ upon 1 MeV Kr^{2+} ion irradiation at (a) 480 K, (b) 520 K, and (c) 600 K. The ion fluences and doses in dpa are given at the top of each dark field TEM images.

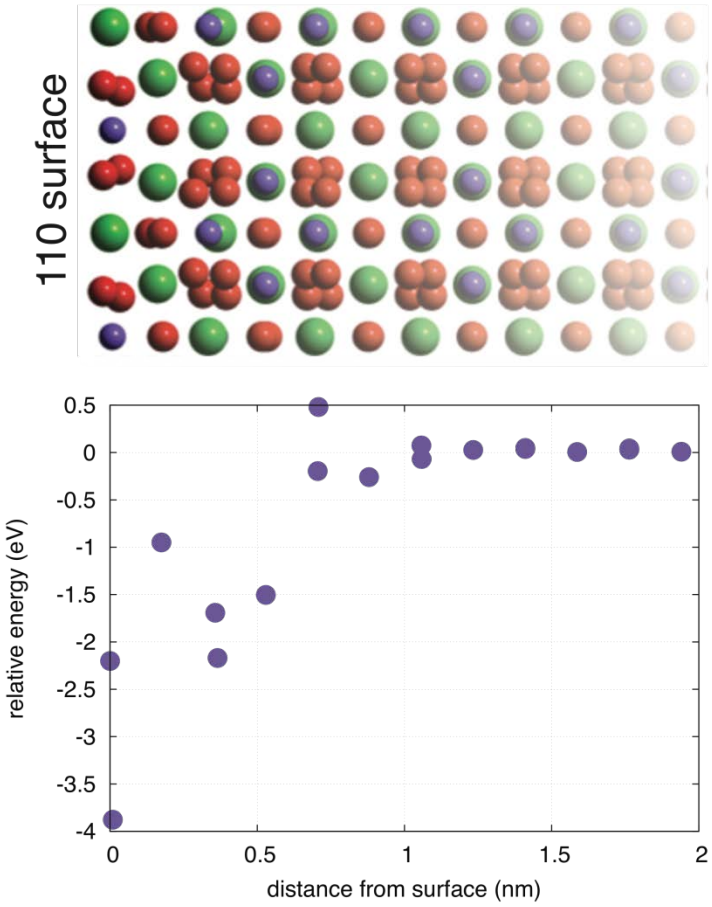

Fig. 7. Calculated relative energy (eV) of a nearest neighbor cation antisite pair formation in $Lu_2Ti_2O_7$ pyrochlore as a function of distance from the (110) surface (located at 0 nm), which is schematically illustrated above the plot.

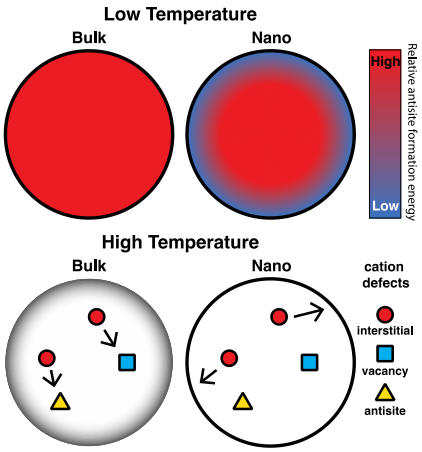

Fig. 8. Schematic of the proposed radiation damage mechanisms that dominate at low and high temperature in bulk versus nanocrystalline pyrochlore. In nanocrystalline pyrochlore, the formation energy of antisites (and other types of defects) is reduced at surfaces, reducing the average formation energy of antisites. At low temperature, where defect thermodynamics dominate the response, this suggests that nanocrystalline pyrochlore is more radiation tolerant than large grained material. In contrast, at high temperature, the cation interstitials that are responsible for healing those defects that lead to amorphization in the bulk are swept away to surfaces in nanocrystalline pyrochlore, eliminating their ability to heal those defects.